Hunting dark matter with X-rays

Franse, J.

3 | Devoted Observations of the Draco Dwarf Spheroidal

Based on
Searching for decaying dark matter in deep XMM-Newton observation of the Draco dwarf spheroidal
Oleg Ruchayskiy, Alexey Boyarsky, Dmytro Iakubovskyi, Esra Bulbul, Dominique Eckert, Jeroen Franse, Denys Malyshev, Maxim Markevitch, Andrii Neronov
Published in *Monthly Notices of the Royal Astronomical Society*

3.1 Introduction

An emission line-like spectral feature at energy $E \sim 3.5$ keV has recently been observed in the long-exposure X-ray observations of a number of dark matter-dominated objects: in a stack of 73 galaxy clusters (Bulbul et al., 2014a) and in the Andromeda galaxy and the Perseus galaxy cluster (Boyarsky et al., 2014a). The possibility that this spectral feature may be the signal from decaying dark matter has sparked a lot of interest in the community, and many dark matter models explaining this signal have been proposed (see e.g. Iakubovskyi (2014) and refs. therein). The signal was subsequently detected in the Galactic Center (Riemer-Sorensen, 2014; Boyarsky et al., 2015; Jeltema & Profumo, 2015; Carlson et al., 2015), in the center of the Perseus galaxy cluster with *Suzaku* (Urban et al., 2015), in a stacked spectrum of a new set of galaxy clusters (Iakubovskyi et al., 2015), but not found in stacked spectra of dwarf spheroidal galaxies (Malyshev et al., 2014), in outskirts of galaxies (Anderson et al., 2015), in the diffuse X-ray background (Figueroa-Feliciano et al., 2015; Sekiya et al., 2015).

There are three classes of non-dark matter explanations: a statistical fluctuation, an unknown systematic effect or an atomic line. Instrumental origins of this signal have been shown to be unlikely for a variety of reasons: the signal is present in the spectra of galaxy clusters in all of *XMM-Newton* detectors and also in *Chandra*, yet it is absent in a very-long exposure *XMM-Newton* (Boyarsky et al., 2014a) or *Suzaku* (Sekiya et al., 2015) blank sky backgrounds. The position of the line in galaxy clusters scales correctly with redshift (Bulbul et al., 2014a; Boyarsky et al., 2014a; Iakubovskyi et al., 2015), and the line has radial surface brightness profiles in the Perseus cluster (except its core (Bul-

bul et al., 2014a)) and Andromeda galaxy (Boyarsky et al., 2014a) consistent with our expectations for decaying dark matter and with the mass distribution in these objects.

The astrophysical explanation of this signal (e.g., an anomalously bright K XVIII line (Bulbul et al., 2014a; Riemer-Sorensen, 2014; Boyarsky et al., 2015; Jeltema & Profumo, 2015; Carlson et al., 2015; Iakubovskyi et al., 2015) or Ar XVII satellite line (Bulbul et al., 2014a), or a Sulfur charge exchange line (Gu et al., 2015)) require a significant stretch of the astrophysical emission models, though they can be unambiguously tested only with the high spectral resolution of the forthcoming *Astro-H* and *Micro-X* (Mitsuda et al., 2014; Koyama et al., 2014; Kitayama et al., 2014; Figueroa-Feliciano et al., 2015; Iakubovskyi, 2015) microcalorimeters.

The dark matter interpretation of the origin of the line allows for a non-trivial consistency check by comparing observations of different objects: the intensity of the line should correlate with the *dark matter column density* – a quantity that is bracketed between roughly $10^2\,M_\odot/\mathrm{pc}^2$ and few $\times\,10^3\,M_\odot/\mathrm{pc}^2$ for all objects from smallest galaxies to larger clusters (Boyarsky et al., 2010a, 2009b). For example, the observation of the 3.5 keV line in M31 and the Perseus cluster puts a *lower limit on the flux* expected from the Galactic Center (GC). On the other hand, the non-detection of any signal in the off-center observations of the Milky Way halo (the blank sky dataset of Boyarsky et al., 2014a) *provides an upper limit* on the possible flux from the GC, given the observational constraints on the DM distribution in the Galaxy. Boyarsky et al. (2015) demonstrated the flux of the 3.5 keV line detected in the GC, falls into this range.

To study this question further, we observed the central $r = 14'$ of the Draco dwarf spheroidal galaxy with *XMM-Newton* with a very deep exposure of 1.4 Msec. Dwarf spheroidal galaxies (dSphs) are the most extreme dark matter-dominated objects known. The observations of thousands of stars in the "classical" dwarf satellites of the Milky Way make possible the determination of their DM content with very low uncertainties, with the Draco dSph being one of the best studied (see Geringer-Sameth et al. (2015) for the latest mass modeling). The relatively small uncertainty on the dark matter column density in Draco and its "faintness" in X-rays due to lack of gas or X-ray binaries allows us to devise a test of the decaying dark matter interpretation of the $\sim$3.5 keV line, as we have a clear prediction of the expected line flux for Draco based on the masses of this galaxy and the other objects.

A clear detection of the $\sim$3.5 keV line in Draco would provide very convincing evidence for the decaying DM interpretation, as there is no known physical process that would produce *the same signal* over such a broad range of objects and environments, with an intensity that scales with the DM content, from galaxy clusters of huge masses and large abundances of hot gas, through spiral galaxies, and then all the way down to dwarf galaxies of very low magnitude and negligible gas content.

The estimated column density within the central $14'$ is a factor of a few lower in dSphs (including Draco) than in the centers of nearby spiral galaxies or clusters (albeit has a much lower uncertainty). Therefore, to achieve the same signal-to-noise for a dSph as for a spiral galaxy for all observationally possible ratios of the DM column density, one would need a prohibitively long observation. The uncertainty in DM content of the galaxies becomes crucial. Therefore, the raw exposure time of the Draco observation (1.4 Msec) has been chosen to match the shortest exposure expected to still allow for detection of the weakest possible line (compatible with previous observations).

In this paper we describe the results of the analysis of these Draco observations. We do find weak positive residuals at the predicted energy above the (carefully-modeled) continuum in the PN spectrum and in one of the two MOS spectra, but at a low statistical significance that allows only an upper limit on the line flux to be set. The upper limit is consistent with most of the previous positive line detections, thus, we *cannot exclude dark matter decay* as origin of the 3.5 keV line.

3.2 Data preparation and analysis

We analysed observations of Draco dSph performed in 2015 by the European Photon Imaging Cameras (EPIC; Strüder et al., 2001; Turner et al., 2001) on-board of the X-ray Multi-Mirror Observatory *XMM-Newton* (Jansen et al., 2001) as a part of the AO-14 campaign (proposal 76480, PI: A. Boyarsky). The 1.4 Ms total requested exposure was divided into 26 observations (Table 3.3). We processed these observations from raw data using Extended Source Analysis Software (ESAS; Kuntz & Snowden, 2008) provided as part of the *XMM-Newton* Science Analysis System SAS v.14.0.0, with calibration files current as of December 1, 2015. Time intervals affected by soft proton flares were rejected using ESAS procedure `mos-filter` with standard spectral cuts. This rejection removed $\sim$30% ($\sim$50%) of raw exposure for MOS (PN) cameras, comparable to other methods described in e.g. Sec. 8.4.1 of Iakubovskyi (2013). While the exposure reduction is significant, our tests showed that the sensitivity to the line does not increase if we use less-rigorous cleaning, because of the resulting increase of the continuum brightness. We excised the unrelated X-ray point sources using the ESAS procedure `cheese`, which masks the sky regions *around the detected point sources* of $\geq$36" radius which corresponds to the removal of $\geq$70% per cent of total encircled energy. For each observation, exposures and fields-of-view after removal of proton flares and point sources are listed in Table 3.3. Spectra and response matrices from MOS and PN cameras produced by ESAS procedure `mos-spectra` were then combined using FTOOL `addspec` and binned with FTOOL `grppha` by 65 eV to have excellent statistics ($\sim 1-2\%$ rms variation per bin obtained from $\gtrsim 2000$ counts per bin in our spectra – comparable to the expected line excess above the continuum) while still resolving the spectral lines. For PN camera, we additionally corrected the obtained spectra for out-of-time events using the standard procedure.

We stress that for our current purpose, given the low expected flux of the spectral line in question and the limited spectral resolution of the CCD detectors, accurate modeling of the continuum emission in the immediate vicinity of the line is crucial. For this, we must account for all the faint detector lines and features that may bias the continuum even at a percent level. We do this by creating a spectral model that includes the detector and sky X-ray background components as described below. We analyse the spectra in the band 2.8–10 keV (for MOS spectra) and 2.8–6.8 + 10–11 keV for PN spectra (to stay well away from the mirror edges found at $E \lesssim 2.5$ keV) using standard X-ray spectral fitting tool `Xspec`. The region 6.8-10 keV was removed from PN camera to avoid modeling very strong instrumental lines (Ni Kα, Cu Kα, Ni Kβ and Zn Kα, see Table 3.1) that cannot be modeled adequately with simple Gaussian profiles at such good statistics. However, adding the high energy bins (at 10-11 keV) allows us to constrain the slope of

the instrumental continuum.

The instrumental background is modeled by a sum of unfolded broken `powerlaw` continuum and several narrow `gaussians` corresponding to bright fluorescent lines originating inside the instrument. Because astrophysical emission from dwarf spheroidal galaxies is negligible (Gizis et al., 1993; Boyarsky et al., 2007b; Jeltema & Profumo, 2008; Riemer-Sorensen & Hansen, 2009; Boyarsky et al., 2010b; Sonbas et al., 2015), the astrophysical model represents the contribution of the Cosmic X-ray background (CXB) as modeled by a folded `powerlaw` continuum. The best-fit values of the flux and powerlaw index of Cosmic X-ray background were allowed to change within 95% CL to the best-fit values from Moretti et al. (2009). Neutral hydrogen absorption column density was fixed to the weighted value $n_H = 2.25 \times 10^{20}$ cm^{-2} obtained from Leiden-Argentine-Bonn survey (Kalberla et al., 2005) in the direction of Draco. The obtained CXB parameters from MOS1, MOS2 and PN are consistent with each other and with those summarized in Moretti et al. (2009) at < 90 % level. Moreover, if one freezes the CXB parameters in PN camera at the level of MOS1/MOS2 or at the level of Moretti et al. (2009) the best-fit normalization of 3.5 keV line in PN camera changes by no more than 10%, much beyond its statistical errors ($\sim$40 %, according to Eq. 3.1). We conclude therefore that the origin of the positive line-like residual at 3.5 keV seen in PN camera is not due to variation of CXB parameters from its 'conventional' level.

To check for possible instrumental gain variations, we split our datasets into three smaller subsets grouped by observation time, see observations 1-9, 10-17, and 18-26 in Table 3.3. For each dataset, we present the average position for Cr Kα and Mn Kα instrumental lines, see Table 3.2 for details. No systematic gain variations across the datasets is detected.

3.3 Results

The extracted spectra are shown in Fig. 3.1. They are dominated by the instrumental and Cosmic (CXB) X-ray backgrounds, which we will carefully model below to see if there is any residual flux at 3.5 keV. As has been stressed in our previous works, the 3.5 keV line feature is so weak that the continuum in its spectral vicinity has to be modeled to a very high precision to be able to detect the line – more precisely than what's acceptable in the usual X-ray observation.

The basic information about the observations is listed in Table 3.3. As a baseline model, we used the combination of Cosmic X-ray Background (extragalatic `powerlaw` folded with the effective area of the instrument) and instrumental background (instrumental `powerlaw` not folded with instrument response, plus several narrow `gaussians` describing fluorescence lines) components. The model parameters are summarized in Table 3.1; they are consistent with previous measurements and are consistent among MOS1, MOS2 and PN cameras. Particular differences of the models among individual cameras are described below.

Parameter	MOS1	MOS2	PN
CXB `powerlaw` index	$1.40^{+0.32}_{-0.06}$	$1.36^{+0.07}_{-0.08}$	$1.61^{+0.13}_{-0.06}$
CXB `powerlaw` flux at 2-10 keV [10^{-11} erg/sec/cm^2/deg^2]	$1.37^{+0.34}_{-0.67}$	$1.40^{+0.30}_{-0.40}$	$2.03^{+0.38}_{-0.30}$
Instrumental background `powerlaw` index	$0.31^{+0.06}_{-0.05}$	$0.26^{+0.05}_{-0.04}$	$0.36^{+0.03}_{-0.02}$
Extra gaussian line position at $\sim$3.0 keV [keV]	—	$3.045^{+0.032}_{-0.031}$	—
Extra gaussian line flux at $\sim$3.0 keV [10^{-3} cts/s]	—	$0.3^{+0.1}_{-0.2}$	—
K Kα line position [keV]	$3.295^{+0.039}_{-0.046}$	$3.380^{+0.025}_{-0.020}$	—
K Kα line flux [10^{-3} cts/s]	$0.3^{+0.1}_{-0.2}$	$0.5^{+0.1}_{-0.2}$	—
Ca Kα line position [keV]	—	$3.770^{+0.017}_{-0.023}$	—
Ca Kα line flux [10^{-3} cts/s]	—	$0.5^{+0.2}_{-0.1}$	—
Ti Kα line position [keV]	$4.530^{+0.028}_{-0.028}$	—	$4.530^{+0.002}_{-0.014}$
Ti Kα line flux [10^{-3} cts/s]	$0.4^{+0.1}_{-0.1}$	—	$4.6^{+0.4}_{-0.3}$
Cr Kα line position [keV]	$5.420^{+0.005}_{-0.005}$	$5.431^{+0.004}_{-0.005}$	$5.445^{+0.001}_{-0.001}$
Cr Kα line flux [10^{-3} cts/s]	$2.1^{+0.1}_{-0.2}$	$3.7^{+0.2}_{-0.1}$	$11.2^{+0.4}_{-0.3}$
Mn Kα line position [keV]	$5.919^{+0.006}_{-0.008}$	$5.901^{+0.005}_{-0.005}$	$5.910^{+0.014}_{-0.015}$
Mn Kα line flux [10^{-3} cts/s]	$1.8^{+0.1}_{-0.1}$	$3.2^{+0.2}_{-0.1}$	$3.3^{+0.4}_{-0.3}$
Fe Kα line position [keV]	$6.386^{+0.020}_{-0.025}$	$6.424^{+0.006}_{-0.018}$	$6.395^{+0.014}_{-0.013}$
Fe Kα line flux [10^{-3} cts/s]	$1.6^{+0.4}_{-0.5}$	$3.7^{+0.2}_{-1.0}$	$9.7^{+1.1}_{-1.0}$
Fe Kβ line position [keV]	$7.128^{+0.038}_{-0.025}$	$7.148^{+0.037}_{-0.038}$	n/i[a]
Fe Kβ line flux [10^{-3} cts/s]	$0.5^{+0.1}_{-0.1}$	$0.4^{+0.1}_{-0.2}$	n/i[a]
Ni Kα line position [keV]	$7.460^{+0.016}_{-0.015}$	$7.479^{+0.006}_{-0.008}$	n/i[a]
Ni Kα line flux [10^{-3} cts/s]	$0.8^{+0.2}_{-0.1}$	$2.2^{+0.1}_{-0.2}$	n/i[a]
Cu Kα line position [keV]	$8.021^{+0.029}_{-0.026}$	$8.045^{+0.015}_{-0.025}$	n/i[a]
Cu Kα line flux [10^{-3} cts/s]	$0.5^{+0.1}_{-0.1}$	$0.9^{+0.2}_{-0.1}$	n/i[a]
Ni Kβ line position [keV]	$8.251^{+0.039}_{-0.037}$	$8.267^{+0.042}_{-0.052}$	n/i[a]
Ni Kβ line flux [10^{-3} cts/s]	$0.4^{+0.1}_{-0.2}$	$0.4^{+0.1}_{-0.2}$	n/i[a]
Zn Kα line position [keV]	$8.620^{+0.023}_{-0.016}$	$8.629^{+0.021}_{-0.015}$	n/i[a]
Zn Kα line flux [10^{-3} cts/s]	$0.8^{+0.1}_{-0.1}$	$0.9^{+0.2}_{-0.1}$	n/i[a]
Au Lα line position [keV]	$9.716^{+0.007}_{-0.005}$	$9.710^{+0.009}_{-0.004}$	n/i[a]
Au Lα line flux [10^{-3} cts/s]	$3.0^{+0.2}_{-0.2}$	$3.4^{+0.1}_{-0.2}$	n/i[a]
Overall quality of fit (χ^2/dof)	73.8/86	79.3/75	47.0/58

Table 3.1: Model parameters for MOS1, MOS2 and PN cameras including positions and fluxes of instrumental line candidates.
[a] In PN, bright instrumental lines at 7-10 keV are not included (n/i) to our model due to large residuals appearing when these lines are modeled. Instead, we included high-energy range above 10 keV to our PN to improve the instrumental continuum modeling.

Parameter	Cr Kα position [keV]	Mn Kα position [keV]
MOS1, obs. 1-9	$5.427^{+0.013}_{-0.012}$	$5.922^{+0.013}_{-0.013}$
MOS1, obs. 10-17	$5.416^{+0.009}_{-0.006}$	$5.914^{+0.011}_{-0.010}$
MOS1, obs. 18-26	$5.402^{+0.014}_{-0.011}$	$5.930^{+0.031}_{-0.031}$
MOS1, full dataset	$5.420^{+0.005}_{-0.005}$	$5.919^{+0.006}_{-0.008}$
MOS2, obs. 1-9	$5.436^{+0.005}_{-0.007}$	$5.895^{+0.009}_{-0.009}$
MOS2, obs. 10-17	$5.431^{+0.005}_{-0.006}$	$5.918^{+0.008}_{-0.007}$
MOS2, obs. 18-26	$5.431^{+0.008}_{-0.007}$	$5.888^{+0.008}_{-0.008}$
MOS2, full dataset	$5.431^{+0.004}_{-0.005}$	$5.901^{+0.005}_{-0.005}$
PN, obs. 1-9	$5.443^{+0.002}_{-0.013}$	$5.916^{+0.042}_{-0.036}$
PN, obs. 10-17	$5.431^{+0.014}_{-0.001}$	$5.955^{+0.059}_{-0.059}$
PN, obs. 18-26	$5.446^{+0.013}_{-0.001}$	$5.909^{+0.016}_{-0.016}$
PN, full dataset	$5.445^{+0.001}_{-0.001}$	$5.910^{+0.014}_{-0.015}$

Table 3.2: Best-fit positions and 1σ errors for Cr Kα and Mn Kα instrumental lines detected in three different subsets of our dataset grouped by the time of observation, see observations 1-9, 10-17 and 18-26 from Table 3.3. The lines position listed for our full dataset also listed in Table 3.1 is shown for comparison. No systematic gain variations across the datasets is detected.

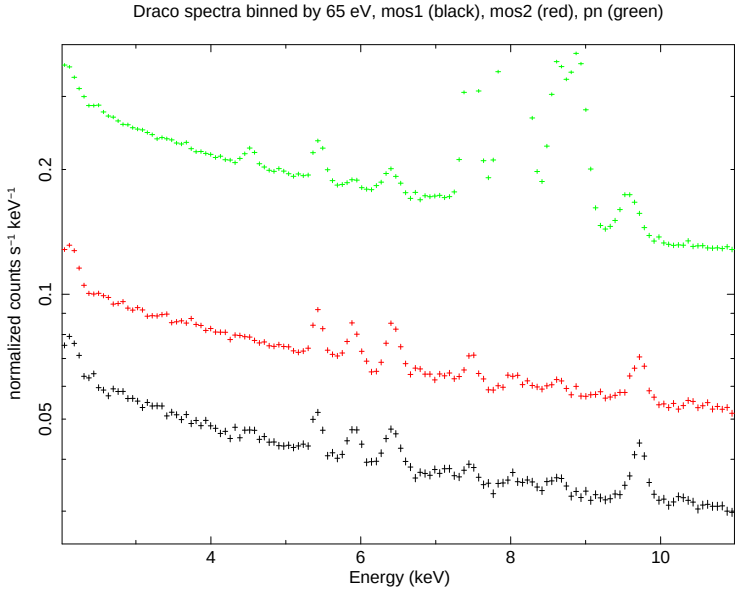

Figure 3.1: Spectra of Draco dwarf spheroidal seen by MOS1 (black), MOS2 (red) and PN (green) cameras.

	ObsID	Observation date	Cleaned exposure [ksec]	Cleaned FoV [arcmin^2]
		MOS1/MOS2/PN	MOS1/MOS2/PN	
28	0764800101	2015-03-18	31.6/36.0/12.4	320.7/573.7/553.1
29	0764800301	2015-03-26	23.9/28.2/13.5	319.4/575.2/549.8
30	0764800401	2015-03-28	41.3/42.0/30.5	316.8/571.6/545.3
31	0764800201	2015-04-05	26.1/27.6/17.2	315.4/571.5/549.0
32	0764800501	2015-04-07	47.5/49.5/24.7	314.6/567.1/543.4
33	0764800601	2015-04-09	52.5/52.0/38.9	314.2/568.5/542.9
34	0764800801	2015-04-19	25.4/29.3/12.8	320.3/573.7/554.8
35	0764800901	2015-04-25	36.0/44.2/16.5	318.3/574.3/550.7
36	0770180101	2015-04-27	34.1/35.9/20.9	323.8/579.5/548.2
37	0770180201	2015-05-25	51.9/53.4/32.4	314.2/569.4/541.2
38	0764800701	2015-06-15	54.2/54.5/47.7	312.9/566.3/530.0
39	0770180401	2015-06-18	50.5/50.1/40.3	315.4/564.1/536.2
40	0770180301	2015-07-01	52.5/54.8/47.4	311.4/565.9/535.2
41	0770180501	2015-07-31	49.1/50.2/41.0	315.6/571.0/538.9
42	0770180701	2015-08-22	38.0/38.5/25.2	320.1/572.8/546.8
43	0770180601	2015-09-01	46.6/49.0/26.2	318.5/573.9/548.7
44	0770180801	2015-09-03	64.2/65.8/48.0	322.1/577.9/537.7
45	0770190401	2015-09-11	50.1/50.0/40.2	328.2/583.9/565.8
46	0770190301	2015-09-21	22.5/24.8/11.6	324.1/578.6/554.0
47	0770190101	2015-09-23	18.1/19.5/0.9	334.1/590.5/566.5
48	0770190201	2015-09-25	18.8/20.1/9.3	322.3/579.5/553.9
49	0770190501	2015-10-11	30.8/31.5/20.3	320.2/576.8/542.9
50	0770180901	2015-10-13	19.2/20.8/11.4	324.6/579.1/560.9
51	0770190601	2015-10-15	7.6/11.2/4.6	329.1/584.0/553.8
52	0770190701	2015-10-17	43.7/45.0/35.5	320.5/572.8/537.4
53	0770190801	2015-10-19	31.7/32.5/22.4	326.2/583.2/547.2
	Total		967.8/1016.1/651.8	318.9/573.5/543.9

Table 3.3: Cleaned exposures and fields-of-view for 26 AO14 observations of Draco dSph used in our analysis, see Appendix 3.2 for details. Notable difference between MOS1 and MOS2 fields of view is due to micrometeoroid damages in MOS1, see e.g. Abbey et al. (2006).

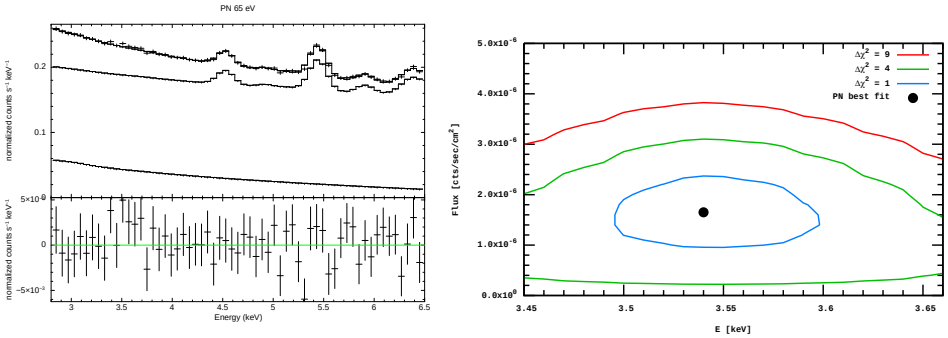

Figure 3.2: Left panel: PN spectrum with *unmodeled* feature at 3.54 keV. Also shown instrumental (upper) and astrophysical (lower) components of the background model. Right panel: Best fit value (black square) and $\Delta\chi^2 = 1, 4, 9$ contours for the line in the PN camera.

3.3.1 Line detection in PN camera

We obtained an excellent fit to the EPIC PN spectrum, with $\chi^2 = 47.0$ for 58 d.o.f. (Table 3.1). The spectrum shows a faint line-like residual at the right energy, $E = 3.54^{+0.06}_{-0.05}$ keV. Its flux is

$$F_{\rm PN} = \begin{cases} 1.65^{+0.67}_{-0.70} \times 10^{-6}\,{\rm cts/sec/cm^2} \\ 3.0^{+1.23}_{-1.29} \times 10^{-9}\,{\rm cts/sec/cm^2/arcmin^2} \end{cases} \quad (3.1)$$

(where the bottom value corresponds to the surface brightness). The improvement of fit when adding the line is $\Delta\chi^2 = 5.3$ for 2 additional d.o.f.. Thus, the detection has a relatively low significance of 2.3σ. The PN spectrum with the unmodeled line-like residual together with the $\Delta\chi^2 = 1, 4, 9$ contours is shown in Figure 3.2. In this Figure, we show only 2.8-6.5 keV range for clarity, while the fit includes higher energies, as described in Appendix 3.2.

3.3.2 MOS cameras

Next we turn to MOS1 and MOS2 cameras. In MOS2 camera, we detected line-like residuals at ~ 3.38 keV (significance 3.2σ) and ~ 3.77 keV (significance 3.5σ), see Table 3.1 in Appendix 3.2. The positions of these residuals are consistent with K Kα and Ca Kα fluorescent lines, respectively. These fluorescent lines have not been previously detected in the MOS cameras, but have been detected in the PN camera with the enhanced calibration source (the so-called `CalClosed` mode, see Fig. 6 of Strüder et al. (2001) for details). Another line-like residual at ~ 3.05 keV is visible (in the MOS2 spectrum only) at a 1.9σ significance; we could not identify it, though its energy is consistent with L and M lines of several heavy metals. In order to get as accurate a continuum model as possible, we have included these weak detector lines as narrow `gaussian` components in our spectral model.

Camera	PN flux $[10^{-6}\,\mathrm{cts/sec/cm^2}]$	Predicted flux $[10^{-6}\,\mathrm{cts/sec/cm^2}]$	$\Delta\chi^2$
MOS1, PN best-fit	1.65	0.97	1.58
MOS2, PN best-fit	1.65	1.74	2.23
MOS1, PN 1σ lower	0.95	0.56	0.27
MOS2, PN 1σ lower	0.95	1.00	0.25

Table 3.4: Consistency check of MOS1 and MOS2 cameras with rescaled flux from PN camera. Line position is allowed to vary within 1σ bound for PN, i.e. 3.49–3.60 keV. See also Figures 3.3 and 3.4.

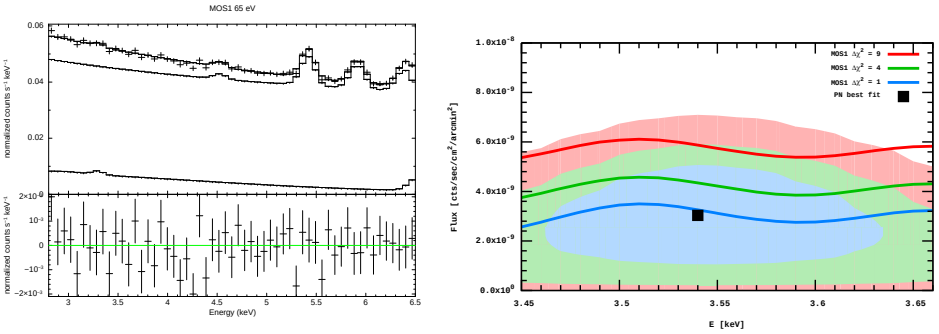

Figure 3.3: *Left panel:* MOS1 spectrum and residuals. *Right panel:* $\Delta\chi^2 = 1, 4, 9$ contours from the MOS1 camera (thick lines). The PN camera contours with $\Delta\chi^2 = 1, 4, 9$ are shown as shaded regions (identical to the contours in Fig. 3.2).

The MOS1 camera reveals no other lines in the region 3–4 keV, see left panel in Figure 3.3. The MOS2 camera has a hint of a residual ($\Delta\chi^2 = 1.2$) in the position 3.60 ± 0.07 keV, see left panel in Figure 3.4. Assuming that the line detected in the PN camera is a physical line, we rescale the PN flux, given by Eq. (3.1), according to the ratio of MOS1 and MOS2 FoV to that of the PN camera (see Table 3.3). Table 3.4 shows the change in the χ^2 (after running the new fit) when one adds a line with a fixed flux to the spectrum of MOS1 and MOS2 (allowing its position to vary within $\pm 1\sigma$ – from 3.49 to 3.60 keV). Clearly the non-observation in MOS1 and MOS2 are consistent with PN observation at $\lesssim 1\sigma$ level.

3.3.3 Common fit of MOS1, MOS2 and PN cameras

Having shown that the three XMM cameras are consistent with each other, we now perform a common fit of all three. We kept the ratio of the `gaussian` normalisations at $\sim$ 3.5 keV fixed to the ratios of the corresponding FoVs. This is justified if the surface brightness is uniform across the FoV of the XMM cameras. We estimated that assuming instead cuspy Navarro-Frenk-White dark matter profile, the expected surface brightness of 3.5 keV features caused by decaying dark matter differs

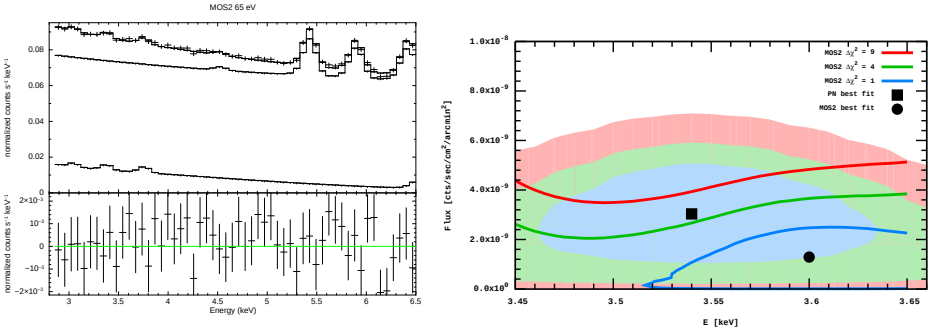

Figure 3.4: *Left panel:* MOS2 spectrum with *unmodeled* feature at ∼3.5 keV and residuals. *Right panel:* $\Delta\chi^2 = 1, 4, 9$ contours from the MOS2 camera (thick lines) and the best fit value (black circle). The PN camera contours with $\Delta\chi^2 = 1, 4, 9$ are shown as shaded regions (identical to the contours in Fig. 3.2).

between the cameras by no more than 15%[1]. This different scaling of the signal between cameras would affect the results of our combined fit by less than 5%. The common fit finds a positive residual with $\Delta\chi^2 = 2.9$ at $E = 3.60 \pm 0.06$ keV and the flux $F = 1.3^{+0.9}_{-0.7} \times 10^{-9}\,\mathrm{cts/sec/cm^2/arcmin^2}$. The resulting flux is compatible with the best-fit PN flux (Eq. 3.1) at a 2σ level.

3.4 Discussion

We analysed 26 observations of Draco dSph performed with the *XMM-Newton* during its AO14 programme. We find a 2.3σ significant positive line-like residual at $E = 3.54 \pm 0.06$ keV in the PN spectrum. A positive 1σ residual is also seen at $E = 3.60 \pm 0.07$ keV with a flux of $F_{\mathrm{MOS2}} = (0.76 \pm 0.66) \times 10^{-6}\,\mathrm{cts/sec/cm^2}$. Their centroids are within 1σ as the right panel of Fig. 3.4 illustrates. The MOS1 camera had the lowest statistics due to the loss of two CCDs. It does not show the line but the absence of the signal is consistent with PN and MOS2 at the 1σ level. The common fit of MOS1, MOS2 and PN camera performed in Sec. 3.3.3 does not show the presence of a significant positive residual at ∼3.5 keV. As it is unclear how the common fit is affected by the uncertainties of cross-calibration between the three cameras, and because we are conservatively interested in this work in exclusion rather than detection, we will use as our main result the 2σ upper bound from the common fit $F_{2\sigma} < 2.9 \times 10^{-9}\,\mathrm{cts/sec/cm^2/arcmin^2}$, which approximately coincides with the best-fit PN flux, see Fig. 3.5.

[1] While FoV of MOS1 is smaller than that of MOS2 by 44%, this decrease is largely compensated by the fact that *non-central* CCDs are shut down. So the observation of the central densest part of Draco is not affected.

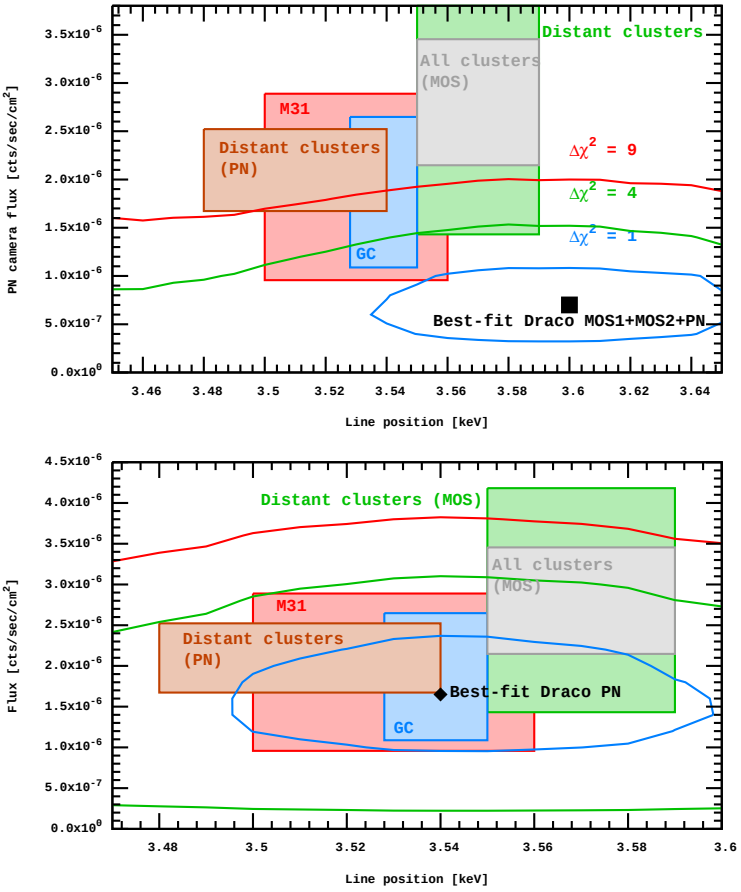

Figure 3.5: *Top:* Common fit to the MOS1, MOS2, and PN cameras (see text for details). The normalization of the 3.5 keV line between cameras is fixed according to the $\Omega_{\rm fov}$ ratios (see Table 3.3). Filled rectangles show the range of fluxes predicted from previous works. The sizes of the regions take into account $\pm 1\sigma$ errors on the measured line fluxes and positions. The height of the rectangles also reflects additional spread in expected DM signals from the specified objects. The previous bounds are based on: Bulbul et al. (2014a) ("All clusters" and "Distant clusters" samples), Boyarsky et al. (2014a) ("M31") and Boyarsky et al. (2015) ("GC"). In particular, for "All clusters" and "Distant clusters" samples, we included an additional 20% uncertainty on its expected DM signal compared to the average values shown in Table 5 of Bulbul et al. (2014a), see Sec. 4.1.2 of Vikhlinin et al. (2009) for detailed discussion. *Bottom:* same as the left panel, but showing the Draco best fit for the PN camera only and the corresponding $\Delta\chi^2$ contours (note the different x and y ranges).

3.4.1 Implications for dark matter decay lifetime

If one interprets this signal as a line from the dark matter decay, its flux is related to the dark matter particle's lifetime τ_{DM} via

$$F = \frac{M_{\rm fov}}{4\pi D_L^2}\frac{1}{\tau_{DM} m_{DM}} = \frac{\Omega_{\rm fov}}{4\pi} S_{DM} \frac{1}{\tau_{DM} m_{DM}} \tag{3.2}$$

where m_{DM} is the DM particle mass (equal to $2 \times E_{\rm line}$), $M_{\rm fov}$ is the DM mass in the field-of-view of the camera, D_L is the luminosity distance, and in the second equality we introduced the *average DM column density*, S_{DM} within the FoV $\Omega_{\rm fov}$.

The expected DM signal from Draco dSph is estimated based on the most recent stellar kinematics data, modeled in Geringer-Sameth et al. (2015). The average column density of Draco within the central $14'$ is $S_{\rm Dra} = 168\,{\rm M}_\odot/{\rm pc}^2$ (with a typical error of $\sim 20\%$; Geringer-Sameth et al., 2015). An additional contribution from the Milky Way halo in the direction of the Draco dSph was adopted at the level of $S_{\rm MW} = 93\,{\rm M}_\odot/{\rm pc}^2$ – based on the profile of Weber & de Boer (2010). The scatter in the values of the MW column density ranges from $56\,{\rm M}_\odot/{\rm pc}^2$ (Xue et al., 2008) to $141\,{\rm M}_\odot/{\rm pc}^2$ (Nesti & Salucci, 2013). The resulting column density we adopt in the direction of Draco is $S_{\rm Dra} = 261^{+82}_{-65}\,{\rm M}_\odot/{\rm pc}^2$.

The corresponding lifetime, inferred from the Draco PN camera observation is $\tau_{\rm Dra} = (5.1 - 21.9) \times 10^{27}{\rm sec}$ depending on dark matter column densities in the direction of Draco:

$$\tau_{\rm Dra} = \begin{cases} 9.6^{+7.1}_{-2.8} \times 10^{27}{\rm sec} & S_{\rm Dra} = (168+93){\rm M}_\odot/{\rm pc}^2 \\ 7.2^{+5.3}_{-2.1} \times 10^{27}{\rm sec} & S_{\rm Dra} = (140+56){\rm M}_\odot/{\rm pc}^2 \\ 12.6^{+9.3}_{-3.7} \times 10^{27}{\rm sec} & S_{\rm Dra} = (202+141){\rm M}_\odot/{\rm pc}^2 \end{cases} \tag{3.3}$$

3.4.2 Comparison with the previous studies of the 3.5 keV line

Is this lifetime of this line compatible with the previous observations of 3.5 keV line? The answer is affirmative (see Fig. 3.5). The comparison with the previous detection in the central $14'$ of the Andromeda galaxy (M31) depends on both uncertainty of the flux measurement and the column density in the direction of the central part of M31, $S_{\rm M31}$. The DM column density in the central $14'$ has been estimated in Boyarsky et al. (2008a, 2010b, 2014a) and references therein. In this work, we adopt two values of $S_{\rm M31}$: $S_{\rm M31,med} = 600\,{\rm M}_\odot/{\rm pc}^2$ (based on profile from Widrow & Dubinski, 2005) and $S_{\rm M31,max} = 1000\,{\rm M}_\odot/{\rm pc}^2$ (based on Geehan et al. (2006); Tempel et al. (2007), see Boyarsky et al. (2008a, 2010b) for the discussion of various profiles). The typical errors on M31 column densities are at the order of 50%. Notice, that a maximal disk large core profile of Corbelli et al. (2010) having $S \approx 120\,{\rm M}_\odot/{\rm pc}^2$ would be incompatible with DM interpretation of the signal. The predicted lifetime would be too short to be consistent with the strength of the signal. This reiterates the conclusion, already made in Boyarsky et al. (2015) – the dark matter interpretation of the 3.5 keV line holds only if the density profiles of spiral galaxies (M31 and Milky Way) are cuspy.

The DM distributions in the Galactic Center region have been summarized in Boyarsky et al. (2015). As a DM column density proxy, we used the distribution of Smith et al. (2007) that gives $S_{\rm GC} = 3370\,{\rm M}_\odot/{\rm pc}^2$. The spread of allowed values of column

Object/ Camera	Observed flux $[10^{-6}\,\mathrm{cts/sec/cm^2}]$	S_{DM} $[M_\odot/\mathrm{pc}^2]$	τ_{DM} $[10^{27}\,\mathrm{sec}]$	Predicted flux $[10^{-6}\,\mathrm{cts/sec/cm^2}]$ MOS1	MOS2	PN
M31 (MOS)	$4.9^{+1.6}_{-1.3}$	600	$7.3^{+2.6}_{-1.8}$	$1.28^{+0.42}_{-0.34}$	$2.31^{+0.76}_{-0.61}$	$2.20^{+0.72}_{-0.58}$
		1000	$12.2^{+4.4}_{-3.0}$	$0.77^{+0.25}_{-0.20}$	$1.38^{+0.45}_{-0.37}$	$1.32^{+0.43}_{-0.35}$
73 (all) stacked clusters (MOS)	$4.0^{+0.8}_{-0.8}$	430	$5.7^{+1.7}_{-1.5}$	$1.65^{+0.59}_{-0.38}$	$2.98^{+1.06}_{-0.68}$	$2.82^{+1.01}_{-0.65}$
69 (distant) stacked clusters (MOS)	$2.1^{+0.4}_{-0.5}$	255	$6.8^{+2.1}_{-2.1}$	$1.38^{+0.43}_{-0.43}$	$2.50^{+0.77}_{-0.77}$	$2.36^{+0.73}_{-0.73}$
Perseus with core (MOS)	$52.0^{+24.1}_{-15.2}$	682	$0.75^{+0.23}_{-0.27}$	$12.5^{+7.0}_{-2.9}$	$22.7^{+12.8}_{-5.3}$	$21.4^{+12.0}_{-5.0}$
GC (MOS)	24^{+12}_{-11}	3370†	$7.9^{+6.7}_{-2.6}$	$1.19^{+0.58}_{-0.55}$	$2.15^{+1.05}_{-0.99}$	$2.03^{+1.00}_{-0.93}$

Table 3.5: Predicted line flux based on Boyarsky et al. (2015); Boyarsky et al. (2014a); Bulbul et al. (2014a). The value for the Draco-deduced lifetime, τ_{Dra} is show in Eq. (3.3).
†: from Smith et al. (2007)

density for the Galactic Center distributions is larger than an order of magnitude, see Fig. 2 of Boyarsky et al. (2015).

Lovell et al. (2015) analysed Milky Way-like halos in the Aquarius simulation, identifying DM halos that could be considered as hosting Draco dSph. It was found that the best agreement between the simulations and observational constraints is for $\tau \sim (6-10)\times 10^{27}$ sec (with which the Draco-deduced lifetime from Eq. 3.3 is fully consistent). They also predicted the ratio of fluxes $F_{\mathrm{Dra}}/F_{\mathrm{GC}}$ to peak at 0.09 with the scatter ranging from 0.04 to 0.2 (95% range). Again, the ratio of the fluxes (~ 0.07) inferred in this paper based on Draco PN data is close to the most probably value predicted by Lovell et al. (2015).

The dark matter column density of the combined sample of galaxy clusters is given by Table 5 of Bulbul et al. (2014a). For the sample of "all distant clusters" considered here, the mean value of DM column density is $S_{\mathrm{clusters}} = 255\,\mathrm{M}_\odot/\mathrm{pc}^2$ and we assign an additional 20% error to this data according to Sec. 4.1.2 of Vikhlinin et al. (2009). Notice that the relative errorbars on individual central column densities are of the order ~ 2, see e.g. Table I of Iakubovskyi et al. (2015). The resulting lifetime is again listed in Table 3.5 and is consistent with our measurements.

Finally, a number of works (Bulbul et al., 2014a; Urban et al., 2015; Boyarsky et al., 2015; Tamura et al., 2015) already observed that the line from the central region of Perseus galaxy cluster is too strong to be compatible with other detections. This signal can only be reconciled with the simple decaying DM hypothesis either if there is a strong additional emission from the atomic lines (e.g., Ar XVII satellite line; Bulbul et al., 2014a) in the central region, or if there is a clump of dark matter, making the central column density much larger than estimated based on the temperature profiles (Bulbul et al., 2014a). The forthcoming *Astro-H* mission (Kitayama et al., 2014; Mitsuda et al., 2014; Takahashi et al., 2012) will be able to resolve the issue with the origin of the emission from the Perseus center, both in core and outskirts, as well as in other bright clusters. On the other hand, outskirts of the Perseus cluster, considered in Boyarsky et al. (2014a) are compatible with the decaying DM interpretation for lifetimes up to 8×10^{27} sec, compatible with Draco-deduced lifetime within 1σ.

3.4.3 Comparison with another recent analysis of Draco extended dataset

In a recent paper (Jeltema & Profumo, 2016, JP16 in what follows), different results of the analysis of the same Draco dSph data have been reported claiming that the dark matter interpretation of the 3.5 keV line is excluded at 99% CL. It is difficult to explain the discrepancies with our results without knowing the details of their data analysis. But we expect that the combination of the following factors may be important here. *(i)* The continuum model of JP16 does not include the extragalactic `powerlaw` component, which affects the shape of the continuum in the 3–4 keV range at the level of a few % in a non-trivial, non-monotonic way due to the energy dependence of the effective area. *(ii)* The lines at $\sim$ 3.3 keV and 3.7 keV are detected but unmodeled in JP16. Again, this increases the best-fit continuum level in the energy range 3–4 keV, which would artificially strengthen the upper bound on a 3.5 keV line. *(iii)* JP16 give the highest weight to their more stringent MOS upper limit. As we see in our spectra, the PN camera shows a positive $\sim 2\sigma$ residual at the expected line energy. When searching for weak signals at or below the telescope sensitivity, it is statistically proper to combine results from the independent detectors (provided they are mutually consistent), as we do. There is no reason to neglect the PN constraint – especially since in this case it is the most sensitive camera of the three, even with the shortest clean exposure.